Strong-field ionization, rescattering, and target structure imaging with vortex electrons

Oleg I. Tolstikhin[*]
Moscow Institute of Physics and Technology, Dolgoprudny 141700, Russia

Toru Morishita[†]
Institute for Advanced Science, The University of Electro-Communications, 1-5-1 Chofu-ga-oka, Chofu-shi, Tokyo 182-8585, Japan

(Received 12 February 2019; published 17 June 2019)

Manifestations of and possibilities related to vortex electrons in strong-field physics are discussed. We present a theory which extends the foundation of a powerful method of target structure and dynamics imaging to vortex electrons. The theory enables one to extract the differential cross section (DCS) for elastic scattering of a *vortex* electron on the parent ion—a collision property introduced here—from the observable photoelectron momentum distribution (PEMD). We illustrate this by considering strong-field ionization from π orbitals in two atoms, Xe and He^+, and a molecule, O_2. The vortex DCS is shown to be sensitive to the target structure. The PEMDs formed by vortex electrons are predicted to be sensitive to the chirality of the target. Extracting vortex DCSs from experimental PEMDs may open a new avenue for rescattering photoelectron spectroscopy.

DOI: 10.1103/PhysRevA.99.063415

I. INTRODUCTION

In quantum mechanics, a freely moving electron may have a nonzero projection of its orbital angular momentum on the direction of propagation. Recently, such vortex wave-packet states have been discussed theoretically [1,2] and relativistic vortex electron beams have been created experimentally [3–5]. The wave function of a vortex electron has a helical phase front, with the probability current density spiraling about the quantization axis, and turns to 0 along the axis. This intrinsic structure strikingly differs from that for ordinary electrons described by wave functions with a locally plane phase front and laminar current flow. One therefore can expect that vortex electrons will demonstrate unusual behavior and properties at a fundamental level, which has naturally aroused much interest. Indeed, unusual features in collision [6–10] and radiation [11–13] processes with vortex electrons and in their interaction with magnetic [14] and electromagnetic [15,16] fields and matter [17] were predicted. The current state of this rapidly developing field and parallels with optical vortices [18] are reviewed in Refs. [19–21].

In this paper we explore possibilities related to vortex electrons in strong-field physics [22]. Free nonrelativistic vortex electrons can be produced by strong-field ionization from bound vortex states—orbitals in linear molecules having a nonzero azimuthal quantum number m. This takes place if the molecule is aligned along a linearly polarized ionizing laser field. An electron released by the field returns to the parent ion and undergoes rescattering after the field changes sign [23]. The value of m is conserved during the evolution, so rescattering occurs with a vortex incident wave. Rescattered photoelectrons carry information about the collision process, and this is encoded in the photoelectron momentum distribution (PEMD) [24,25]. Imaging molecular structure and dynamics by extracting this information from observable PEMDs is the essence of rescattering photoelectron spectroscopy. In particular, a powerful method enabling one to extract the differential cross section (DCS) for electron-ion elastic scattering proposed in Ref. [24] and demonstrated by the analysis of experiments on atoms [26,27] and molecules [28–31] and for the $(e, 2e)$ process [32] has been established [33]. Here, we generalize this method to vortex electrons. Importantly, the DCS in this case is a collision property characterizing elastic scattering of *vortex* electrons. As far as we know, such DCSs have never been discussed theoretically or measured experimentally. The perspective to access this property through strong-field PEMDs opens a new avenue for rescattering photoelectron spectroscopy. The feasibility of this is supported by recent experiments [34,35] to which we return below.

The paper is organized as follows. The adiabatic theory of rescattering for vortex electrons is developed in Sec. II. The theory is illustrated by calculations for two atoms, Xe and He^+, and a diatomic molecule, O_2, in Sec. III. Section IV summarizes our results.

II. THEORY

We consider a linear molecule treated in the single-active-electron approximation. The molecule is assumed to be aligned along the z axis of the laboratory frame. The interaction of the active electron with the molecular ion is described by an axially symmetric potential $V(\rho, z)$ in cylindrical coordinates (ρ, φ, z). The electron is initially bound in an orbital with energy E_m and wave function $\phi_m(\rho, z)e^{im\varphi}$, where m is the projection of its angular momentum on the molecular axis. The wave function satisfies $\phi_m(\rho \to 0, z) \propto \rho^{|m|}$, so vortex orbitals with $m \neq 0$ have a node along the molecular axis; the difference between the shapes of σ $(m = 0)$ and π $(m = 1)$ orbitals is illustrated in Fig. 1(a). The molecule is irradiated by

[*]tolstikhin.oi@mipt.ru
[†]toru@pc.uec.ac.jp

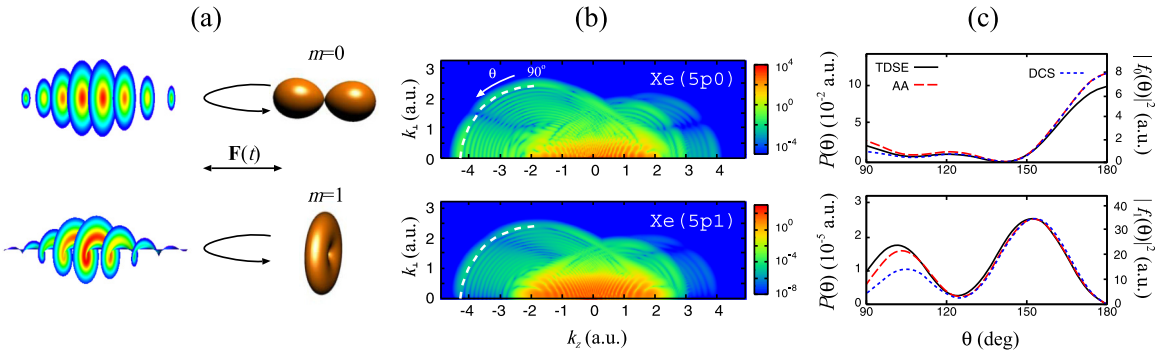

FIG. 1. (a) Schematic of ionization and rescattering for σ ($m = 0$) and π ($m = 1$) orbitals of Xe($5pm$) in a linearly polarized laser field, $\mathbf{F}(t) = F(t)\mathbf{e}_z$. The surfaces on the left show phase fronts of wave packets returning for rescattering. Ionizing orbitals are illustrated on the right. (b) PEMDs $P(k_\perp, k_z)$ for these orbitals generated by a pulse of amplitude $F_0 = 0.1$ and duration $T = 240$ (frequency $\omega \approx 0.052$) obtained by solving the TDSE. Dashed white lines show the backward rescattering caustic $(k_\perp(\theta), k_z(\theta))$ parameterized by the scattering angle θ in the interval $90^\circ \leqslant \theta \leqslant 180^\circ$. The factorization formula, (4), holds in the vicinity of the caustic. (c) Solid black (TDSE) lines show cuts $P(\theta)$ of the PEMDs in (b) along the caustic. Dashed red (AA) lines show results obtained in the adiabatic approximation from Eq. (4). Short-dashed blue (right axis) lines show the DCSs along the caustic $|f_m(\theta)|^2$. DCSs are normalized to the AA results at $\theta = 180^\circ$ for $m = 0$ and at $\theta = 150^\circ$ for $m = 1$.

an intense low-frequency laser pulse linearly polarized along the z axis, with the electric field presented by $\mathbf{F}(t) = F(t)\mathbf{e}_z$. The PEMD $P(k_\perp, k_z)$ in this case is axially symmetric about the k_z axis, where $(k_\perp, \varphi_k, k_z)$ are cylindrical coordinates in the photoelectron momentum space. We solve the time-dependent Schrödinger equation (TDSE) and calculate the PEMD, which is used to demonstrate our idea. On the other hand, we analyze the problem usig the adiabatic theory [36]. The imaging method proposed in Ref. [24] is based on the property of factorization of strong-field PEMDs in a certain region of the photoelectron momentum plane $(k_\perp, k_z)$ into the DCS for electron-ion elastic scattering and a returning photoelectron wave packet (RWP). Recently, we have derived the factorization formula from the adiabatic theory and obtained an analytical expression for the RWP [37], which made the method quantitative. To generalize the method to nonzero m, we need to reconsider the description of the tunneling ionization and rescattering processes and rederive the factorization formula underlying the DCS extraction procedure. We do this following Refs. [36,37]. Atomic units are used throughout.

A. Ionization

In the adiabatic regime, ionization proceeds as if the field were static and equal to the instantaneous laser field [36]. In the presence of a static electric field $\mathbf{F} = F\mathbf{e}_z$, $F \geqslant 0$, the unperturbed bound state turns into a Siegert state (SS) satisfying outgoing-wave boundary conditions [38]. The SS energy $E_m(F)$ is complex; its imaginary part defines the ionization rate $\Gamma_m(F) = -2\,\mathrm{Im}\,E_m(F)$ of the state. The SS eigenfunction contains an outgoing flux at $z \to -\infty$. The transverse momentum distribution (TMD) of electrons in the flux is described by a TMD amplitude $A_m(k_\perp; F)e^{im\varphi_k}$ satisfying $A_m(k_\perp \to 0; F) \propto k_\perp^{|m|}$ [38]. Note that for $m \neq 0$ there are no electrons which tunnel with zero transverse momentum, i.e., along the molecular axis, yet ionization occurs, although at a lower rate than in the case $m = 0$ for the same ionization potential. This can be seen in the weak-field limit, when the rate $\Gamma_m(F)$ and the TMD amplitude $A_m(k_\perp; F)$ are known analytically and related by [39]

$$\Gamma_m(F) = \frac{|m|!}{4\pi}\left(\frac{F}{\varkappa}\right)^{1+|m|}|A_m(F)|^2, \quad F \to 0, \tag{1}$$

where $\varkappa = \sqrt{-2E_m}$ and $A_m(F) = A_m(k_\perp \to 0; F)/k_\perp^{|m|}$. The ratio $A_m(F)/A_0(F)$ for orbitals with equal energies $E_m = E_0$ approaches a constant at $F \to 0$ [39], so the lower rate for $m \neq 0$ results from the higher power of F in Eq. (1). As the laser field slowly varies, the SS adiabatically follows the variation [36]. Its field-dependent properties introduced above become functions of time $E_m(t)$, $\Gamma_m(t)$, and $A_m(t)$ obtained by substituting $F = F(t)$.

B. Rescattering

After tunneling at time t_i in the instantaneous field $F(t_i)$, a wave packet of electrons is driven by the field and returns for rescattering [see Fig. 1(a)] at time t_r defined by the equation $(t_r - t_i)v(t_i) = \int_{t_i}^{t_r} v(t)dt$, where $v(t) = -\int_{-\infty}^{t} F(t')dt'$ is the velocity of a reference electron trajectory [36]. Only electrons with transverse momenta $k_\perp \lesssim a/(t_r - t_i)$ experience rescattering, where a is the range of the potential $V(\rho, z)$ in ρ. In the adiabatic regime [36], such momenta are much smaller than the characteristic width $k_\perp \sim \sqrt{F/\varkappa}$ of the TMD amplitude $A_m(k_\perp; F)$ [39]. Thus, the transverse structure of the wave packet arriving for rescattering in the region $\rho \lesssim a$ is determined by a factor $\rho^{|m|}e^{im\varphi}$. The scattering state produced by such a vortex incident wave propagating with momentum $k\mathbf{e}_z$ is defined by

$$\left[-\tfrac{1}{2}\Delta + V(\rho, z) - \tfrac{1}{2}k^2\right]\phi_m(\mathbf{r}; k) = 0, \tag{2a}$$

$$\phi_m(\mathbf{r}; k)|_{r\to\infty} = \left[(k\rho)^{|m|}e^{ikz - i\gamma \ln k(r-z)} + f_m(k, \theta)\frac{e^{ikr + i\gamma \ln 2kr}}{r}\right]e^{im\varphi}. \tag{2b}$$

Here we have taken into account that the potential may have a Coulomb tail, $V(\rho, z)|_{r\to\infty} = -Z/r$, and $\gamma = Z/k$. The

coefficient $f_m(k,\theta)$ in Eq. (2b) is the scattering amplitude defining the DCS $|f_m(k,\theta)|^2$ for elastic scattering at angle θ. For $m=0$, the scattering state and the DCS defined by Eq. (2) reduce to the usual ones considered in scattering theory [40], but for $m\neq 0$ they represent objects not discussed previously. We mention that Eq. (2) should follow in the appropriate limit from equations used to describe potential scattering of relativistic Bessel vortex electrons [7–10]. However, the limiting procedure is not transparent, while Eq. (2) presents a very simple generalization of the standard scattering problem [40], and this is exactly what we need for the present analysis. It follows from Eq. (2) that $f_m(k,\theta\to\pi)\propto(\pi-\theta)^{|m|}$, i.e., the scattering amplitude for $m\neq 0$ turns to 0 in the backward direction. For a purely Coulomb potential, $V(\rho,z)=-Z/r$, Eq. (2) can be solved analytically and we obtain

$$f_m^{(C)}(k,\theta)=\frac{\Gamma(1+|m|-i\gamma)}{\Gamma(1-i\gamma)}(-i\cot\theta/2)^{|m|}f^{(C)}(k,\theta), \quad (3)$$

where $f^{(C)}(k,\theta)$ is the usual Coulomb scattering amplitude for $m=0$ [40]. The wave packet returns for rescattering with incident momentum $u_f\mathbf{e}_z$, where $u_f=v(t_r)-v(t_i)$ [36]. Therefore rescattering at time t_r is characterized by the amplitude $f_m(u_f,\theta)$.

C. Factorization formula

After rescattering, photoelectrons arrive at a detector. In the general case, there are several trajectories contributing to a given point in the photoelectron momentum plane $(k_\perp,k_z)$. In particular, two trajectories (termed long and short) determine the PEMD in the region where it is dominated by backward rescattered photoelectrons [41]. These trajectories coalesce along a backward rescattering caustic $(k_\perp(\theta),k_z(\theta))$—a line in the $(k_\perp,k_z)$ plane which we parametrize by the scattering angle θ [see dashed lines in Fig. 1(b)]. The caustic is completely determined by the function $F(t)$; explicit formulas are given in Ref. [37]. At the caustic, the kinematic characteristics t_i, t_r, and u_f of the rescattering event become functions of θ [37]. The factorization formula holds in the vicinity of the caustic. It is convenient to introduce curvilinear coordinates $(\theta,\Delta k)$ in this region, with θ defining the position along the caustic and Δk being measured from the caustic along the external normal to it. Following the derivation in Ref. [37] with appropriate modifications dictated by the present vortex structure of the TMD amplitude and scattering state, we obtain in the adiabatic approximation the PEMD

$$P_c(k_\perp,k_z)=|f_m(\theta)|^2W_m(\theta,\Delta k), \quad (4)$$

where $f_m(\theta)=f_m(u_f,\theta)$ is the scattering amplitude at the caustic and

$$W_m(\theta,\Delta k)=|\mathrm{Ai}\,(\alpha(\Delta k-q))|^2\left|\frac{2}{S_r'''}\right|^{2/3}\times\frac{4\pi^2|A_m(t_i)|^2}{u_f^{2|m|}(t_r-t_i)^{3+2|m|}|F(t_i)|}\times\exp\left[-\int_{-\infty}^{t_i}\Gamma_m(t)\,dt\right] \quad (5)$$

is the RWP. Here $\mathrm{Ai}(x)$ is the Airy function, $\alpha=(2/S_r''')^{1/3}|u_f|$, $q=-E_m(t_i)/(t_r-t_i)|F(t_i)|$ is a quantum shift of the caustic, and S_r''' is a function of θ defined in Ref. [37]. Note that the RWP depends on Δk only through the Airy function; all the other factors in Eq. (5) are functions of θ taken at the caustic. Formula (4) generalizes the result in Ref. [37] to arbitrary m. For $m=0$, it has been validated by comparison with TDSE results [37] and successfully applied to the analysis of experiments on atoms [42] and molecules [43]. Below we demonstrate its performance in the vortex case $m\neq 0$.

III. ILLUSTRATIVE CALCULATIONS

We test the theory by calculating PEMDs generated by two-cycle pulses with $F(t)=-F_0\exp[-(2t/T)^2]\cos\omega t$ and $T=4\pi/\omega$. The TDSE is solved using a method described in Ref. [44] generalized to linear molecules aligned along the polarization axis. We have also implemented Eq. (4). The scattering amplitude $f_m(k,\theta)$ is obtained by solving Eq. (2) in spherical coordinates using the slow variable discretization method [45] in combination with the R-matrix propagation technique [46]. The SS properties $E_m(t)$, $\Gamma_m(t)$, and $A_m(t)$ appearing in Eq. (5) are calculated using the method developed in Ref. [38].

We begin with atomic targets. To illustrate the effect of m, we first compare PEMDs resulting from $5pm$ orbitals with $m=0$ and 1 in Xe. The atom is described by the potential defined in Ref. [47]; the same potential was used in Refs. [37,42]. The PEMDs generated by a typical strong-field pulse with amplitude $F_0=0.1$ and frequency $\omega\approx 0.052$ obtained by solving the TDSE are shown in Fig. 1(b). The PEMD for $m=1$ has a smaller magnitude than that for $m=0$, because of the lower ionization rate explained by Eq. (1). For $m=1$, the PEMD has a node at $k_\perp=0$ and its width in $k_\perp$ in the main part of the distribution representing direct photoelectrons is larger than that for $m=0$. The contribution of direct photoelectrons is described by the TMD amplitude [36], so these differences reflect the difference between the TMD amplitudes for $m=0$ and 1. In both cases, there exists a pronounced interference structure produced by the contributions from long and short backward rescattering trajectories in the left part of the distribution. The backward rescattering caustic (shown by dashed lines) goes along the outermost maximum in the structure. Cuts of the PEMDs along the caustic are shown by solid lines in Fig. 1(c). These TDSE results are compared with the results obtained in the adiabatic approximation from Eq. (4) with $\Delta k=0$ (denoted by AA). The very good quantitative agreement between the results for both values of m considered extends the validation of Eq. (4) [37] to nonzero m. In addition, Fig. 1(c) shows the DCSs along the caustic $|f_m(\theta)|^2$. The DCSs for $m=0$ and 1 have quite different shapes, giving different images of the same atomic potential. In particular, the DCS for $m=0$ has a finite value in the backward direction $\theta=180^\circ$, while that for $m=1$ turns to 0 there. The DCSs are normalized to the AA results at certain values of θ, so the difference between the AA and the DCS curves illustrates the dependence of the RWP factor in Eq. (4) on θ.

We next consider the case of a purely Coulomb potential, to test the theory for the most basic system. In Ref. [37], the

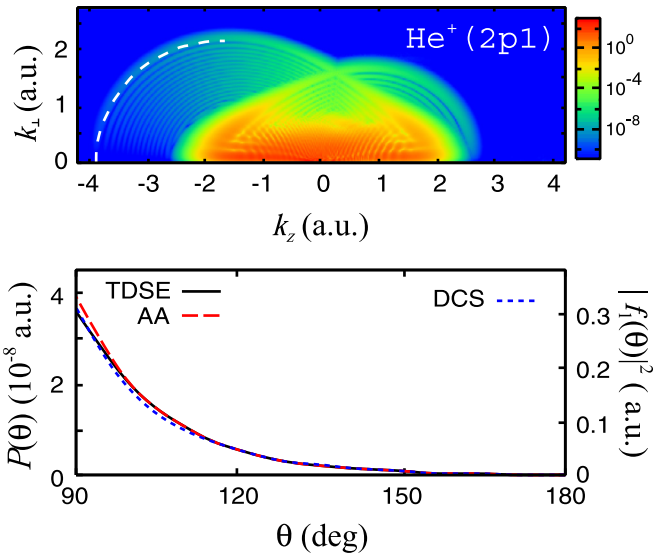

FIG. 2. Top: PEMD $P(k_\perp, k_z)$ for He($2p1$) generated by a pulse with $F_0 = 0.055$ and $T = 400$ ($\omega \approx 0.031$) obtained by solving the TDSE. The dashed line shows the caustic. Bottom: The solid black (TDSE) line shows a cut $P(\theta)$ of the PEMD along the caustic, the dashed red (AA) line shows adiabatic results obtained from Eq. (4), and the short-dashed blue (right axis) line shows the DCS along the caustic $|f_1(\theta)|^2$. The DCS is normalized to the AA results at $\theta = 120^\circ$.

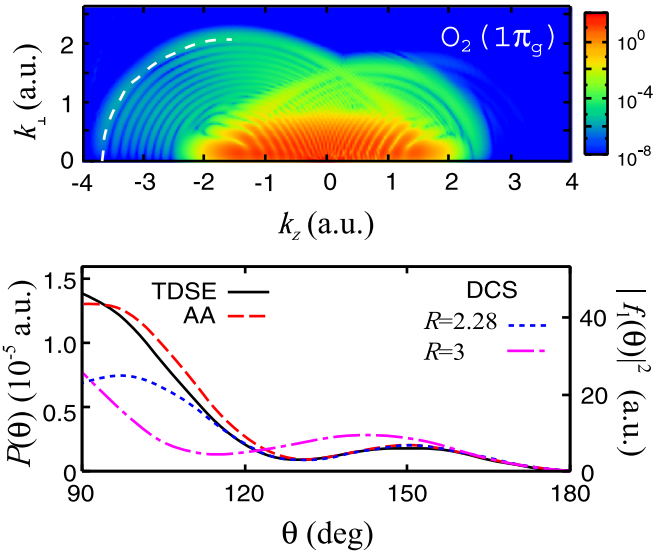

FIG. 3. Similar to Fig. 2, but for the $1\pi_g$ orbital in O_2 at the equilibrium internuclear distance $R = 2.28$. The PEMD is generated by a pulse with $F_0 = 0.08$ and $T = 260$ ($\omega \approx 0.048$). The DCS is normalized to the AA results at $\theta = 150^\circ$. In addition, the dash-dotted magenta (right axis) line in the bottom panel shows the DCS for $R = 3$.

performance of Eq. (4) for $m = 0$ in this case was illustrated by calculations for the $1s$ state of H. To stay within the range of the pulse parameters typical for strong-field physics, here we consider ionization from the $2pm$ orbital with $m = 1$ in He^+. The results obtained for a pulse with $F_0 = 0.055$ and $\omega \approx 0.031$ are shown in Fig. 2. The top and bottom panels in the figure present results similar to those shown in Figs. 1(b) and 1(c), respectively. The DCS in the present case was calculated using Eq. (3). We again see a very good agreement between the TDSE and adiabatic results. The AA and DCS curves are very close to each other, which means that the RWP, (5), taken along the caustic in the present case is almost independent of θ.

We now consider ionization from the highest occupied orbital $1\pi_g$ in a diatomic molecule O_2. The molecule is modeled by a potential given by a sum of two soft-core atomic potentials,

$$V(\rho, z) = -\frac{Z(r_-)}{\sqrt{r_-^2 + \delta^2}} - \frac{Z(r_+)}{\sqrt{r_+^2 + \delta^2}}, \qquad (6)$$

where $r_\pm = |\mathbf{r} \pm \mathbf{R}/2| = \sqrt{\rho^2 + (z \pm R/2)^2}$ are the distances between the active electron and the nuclei located at $\pm\mathbf{R}/2$, $\mathbf{R} = (0, 0, R)$, R is the internuclear distance, $Z(r)$ is a coordinate-dependent effective charge, and $\delta = 0.3$ is a softening parameter. We present $Z(r)$ in the form

$$Z(r) = Z_N - (Z_e - 1)\{1 - [(v/u)(e^{ur} - 1) + 1]^{-1}\} \qquad (7)$$

proposed for modeling atomic potentials in Ref. [48]. This function varies from $Z(0) = Z_N$ to $Z(r \to \infty) = Z_N - Z_e + 1$. We therefore set $Z_N = 8$, for the nuclear charge of O, and $Z_e = 8.5$, so the molecular potential, (6), behaves at $r \to \infty$ as $-Z/r$ with charge $Z = 1$. The parameters $u = 0.95013$ and $v = 2.0509$ in Eq. (7) are chosen such that the energy of the $1\pi_g$ orbital at the equilibrium internuclear distance $R = 2.2819$ is $E_1 = -0.4436$, which reproduces the experimental ionization potential of O_2 [49]. The same approach to constructing one-electron molecular potentials was used in Ref. [43]. It is verified by the good agreement between theoretical and experimental PEMDs demonstrated therein. The results obtained for a pulse with $F_0 = 0.08$ and $\omega \approx 0.048$ are shown in Fig. 3. The agreement between the TDSE and adiabatic results is as good as in the atomic case, which validates Eq. (4) for molecular targets. To illustrate the sensitivity of the DCS for $m = 1$ to the molecular structure, we additionally show in the bottom panel the same DCS calculated for a larger internuclear distance, $R = 3$. The strong dependence of the DCS on R may be used for imaging molecular dissociation process. In Fig. 4, we illustrate the behavior of DCSs $|f_m(k, \theta)|^2$ for O_2 as functions of the incident momentum k and scattering angle θ. The two upper panels calculated for the same internuclear distance $R = 2.28$ illustrate the dependence of the DCS on m. The two lower panels illustrate its dependence on R for $m = 1$. The DCSs shown in Fig. 3 are cuts of those shown in Fig. 4 along the dashed lines representing the caustic. The position of the caustic is determined by the field $F(t)$, so the other parts of the (k, θ) plane in Fig. 4 can be accessed by varying the pulse shape.

Let us return to recent experiments [34,35], where strong-field ionization from molecular orbitals having a nodal surface by a field directed along or close to the surface was observed. The present theory shows that if the field points exactly along a nodal surface, the PEMD is formed by vortex electrons with $m = \pm 1$. If its direction deviates from the surface, a contribution from the $m = 0$ ionization channel appears. Thus, the dependence of the ionization yield on the molecular

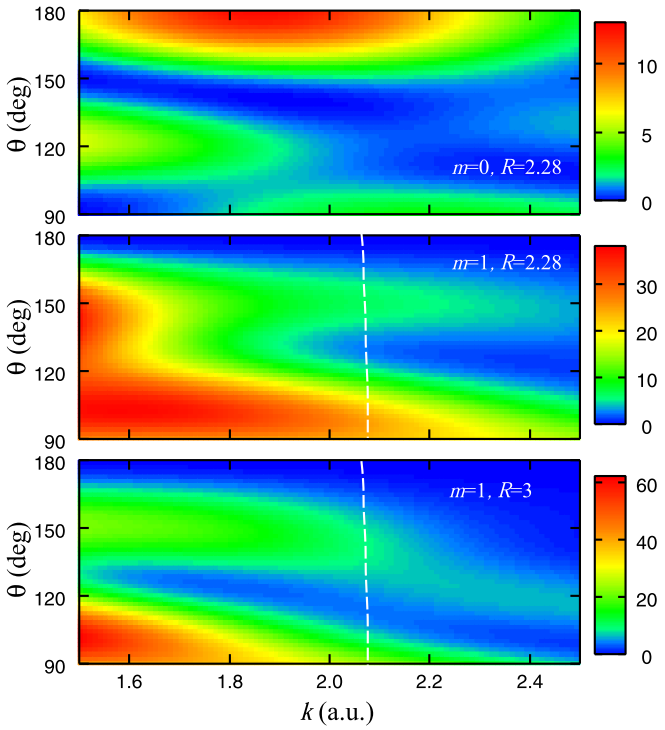

FIG. 4. DCSs $|f_m(k,\theta)|^2$ for O_2 as functions of the incident momentum k and scattering angle θ in a region relevant for applications of Eq. (4). Dashed lines show images of the caustic from Fig. 3. The values of m and the internuclear distance R are indicated.

orientation observed in Ref. [35] can be explained by the interplay of the $m = 0$ and $|m| = 1$ ionization channels. The very fact that the dependence has been observed supports the feasibility of detecting vortex electrons in current experiments.

The most important difference between plane-wave ($m = 0$) and vortex ($m \neq 0$) electrons for rescattering spectroscopy predicted by Eq. (4) consists in the following. The RWP, (5), does not depend on the sign of m, but the DCS for chiral molecules does, and hence so does the PEMD (4). In particular, PEMDs formed by vortex electrons with $m = \pm 1$ in the experimental setup in Refs. [34,35] should be sensitive to the chirality of the target. The present scheme of observing chiral effects in the interaction of vortex electrons with matter via vortex DCSs encoded in strong-field PEMDs has advantages over the approach using externally prepared vortex electron beams [4,17]: (a) the parent ion is automatically located on the beam axis, and (b) subfemtosecond temporal resolution can be achieved [31]. Within strong-field physics, the present scheme enables one to extend the observation of chiral effects from high-order harmonic spectra [50–52] to PEMDs.

IV. SUMMARY OF THE RESULTS

Summarizing, we have introduced a collision property—the DCS for elastic scattering of a vortex electron on the parent ion defined by Eq. (2). We have derived the factorization formula, (4), and shown that it enables one to extract this property from PEMDs generated by strong-field ionization from vortex orbitals in linear molecules. The formula predicts that PEMDs formed by vortex electrons with $m \neq 0$ are sensitive to the chirality of the target. Extracting vortex DCSs from experimental PEMDs may open a new chiral-sensitive window for molecular structure and dynamics imaging in rescattering photoelectron spectroscopy.

ACKNOWLEDGMENTS

O.I.T. acknowledges support from the Ministry of Education and Science of Russia (State Assignment No. 3.873.2017/4.6). T.M. was supported in part by Japan Society for the Promotion of Science KAKENHI Grants No. 16H04029, No. 16H04103, and No. 17K05597.

[1] K. Y. Bliokh, Y. P. Bliokh, S. Savel'ev, and F. Nori, Semiclassical Dynamics of Electron Wave Packet States with Phase Vortices, Phys. Rev. Lett. **99**, 190404 (2007).
[2] I. Bialynicki-Birula and Z. Bialynicka-Birula, Relativistic Electron Wave Packets Carrying Angular Momentum, Phys. Rev. Lett. **118**, 114801 (2017).
[3] M. Uchida and A. Tonomura, Generation of electron beams carrying orbital angular momentum, Nature **464**, 737 (2010).
[4] J. Verbeeck, H. Tian, and P. Schattschneider, Production and application of electron vortex beams, Nature **467**, 301 (2010).
[5] B. J. McMorran, A. Agrawal, I. M. Anderson, A. A. Herzing, H. J. Lezec, J. J. McClelland, and J. Unguris, Electron vortex beams with high quanta of orbital angular momentum, Science **331**, 192 (2011).
[6] I. P. Ivanov, Colliding particles carrying nonzero orbital angular momentum, Phys. Rev. D **83**, 093001 (2011).
[7] R. Van Boxem, B. Partoens, and J. Verbeeck, Rutherford scattering of electron vortices, Phys. Rev. A **89**, 032715 (2014).
[8] V. Serbo, I. P. Ivanov, S. Fritzsche, D. Seipt, and A. Surzhykov, Scattering of twisted relativistic electrons by atoms, Phys. Rev. A **92**, 012705 (2015).
[9] V. P. Kosheleva, V. A. Zaytsev, A. Surzhykov, V. M. Shabaev, and Th. Stöhlker, Elastic scattering of twisted electrons by an atomic target: Going beyond the Born approximation, Phys. Rev. A **98**, 022706 (2018).
[10] A. V. Maiorova, S. Fritzsche, R. A. Müller, and A. Surzhykov, Elastic scattering of twisted electrons by diatomic molecules, Phys. Rev. A **98**, 042701 (2018).
[11] I. P. Ivanov and D. V. Karlovets, Detecting Transition Radiation from a Magnetic Moment, Phys. Rev. Lett. **110**, 264801 (2013).
[12] A. S. Konkov, A. P. Potylitsyn, and M. S. Polonskaya, Transition radiation of electrons with a nonzero orbital angular momentum, JETP Lett. **100**, 421 (2014).
[13] I. P. Ivanov, V. G. Serbo, and V. A. Zaytsev, Quantum calculation of the Vavilov-Cherenkov radiation by twisted electrons, Phys. Rev. A **93**, 053825 (2016).

[14] K. Y. Bliokh, P. Schattschneider, J. Verbeeck, and F. Nori, Electron Vortex Beams in a Magnetic Field: A New Twist on Landau levels and Aharonov-Bohm States, Phys. Rev. X **2**, 041011 (2012).

[15] D. V. Karlovets, Electron with orbital angular momentum in a strong laser wave, Phys. Rev. A **86**, 062102 (2012).

[16] A. G. Hayrapetyan, O. Matula, A. Aiello, A. Surzhykov, and S. Fritzsche, Interaction of Relativistic Electron-Vortex Beams with Few-Cycle Laser Pulses, Phys. Rev. Lett. **112**, 134801 (2014).

[17] S. Lloyd, M. Babiker, and J. Yuan, Quantized Orbital Angular Momentum Transfer and Magnetic Dichroism in the Interaction of Electron Vortices with Matter, Phys. Rev. Lett. **108**, 074802 (2012).

[18] M. R. Dennis, K. O'Holleran, and M. J. Padgett, Singular optics: Optical vortices and polarization singularities, Prog. Opt. **53**, 293 (2009).

[19] J. Harris, V. Grillo, E. Mafakheri, G. C. Gazzadi, S. Frabboni, R. W. Boyd, and E. Karimi, Structured quantum waves, Nat. Phys. **11**, 629 (2015).

[20] K. Y. Bliokh, I. P. Ivanov, G. Guzzinati, L. Clark, R. Van Boxem, A. Béché, R. Juchtmans, M. A. Alonso, P. Schattschneider, F. Nori, and J. Verbeeck, Theory and applications of free-electron vortex states, Phys. Rep. **690**, 1 (2017).

[21] S. M. Lloyd, M. Babiker, G. Thirunavukkarasu, and J. Yuan, Electron vortices: Beams with orbital angular momentum, Rev. Mod. Phys. **89**, 035004 (2017).

[22] F. Krausz and M. Ivanov, Attosecond physics, Rev. Mod. Phys. **81**, 163 (2009).

[23] P. B. Corkum, Plasma Perspective on Strong-Field Multiphoton Ionization, Phys. Rev. Lett. **71**, 1994 (1993).

[24] T. Morishita, A.-T. Le, Z. Chen, and C. D. Lin, Accurate Retrieval of Structural Information from Laser-Induced Photoelectron and High-Order Harmonic Spectra by Few-Cycle Laser Pulses, Phys. Rev. Lett. **100**, 013903 (2008).

[25] M. Meckel, D. Comtois, D. Zeidler, A. Staudte, D. Pavičić, H. C. Bandulet, H. Pépin, J. C. Kieffer, R. Dörner, D. M. Villeneuve, and P. B. Corkum, Laser-induced electron tunneling and diffraction, Science **320**, 1478 (2008).

[26] M. Okunishi, T. Morishita, G. Prümper, K. Shimada, C. D. Lin, S. Watanabe, and K. Ueda, Experimental Retrieval of Target Structure Information from Laser-Induced Rescattered Photoelectron Momentum Distributions, Phys. Rev. Lett. **100**, 143001 (2008).

[27] D. Ray, B. Ulrich, I. Bocharova, C. Maharjan, P. Ranitovic, B. Gramkow, M. Magrakvelidze, S. De, I. V. Litvinyuk, A.-T. Le, T. Morishita, C. D. Lin, G. G. Paulus, and C. L. Cocke, Large-Angle Electron Diffraction Structure in Laser-Induced Rescattering from Rare Ggases, Phys. Rev. Lett. **100**, 143002 (2008).

[28] M. Okunishi, H. Niikura, R. R. Lucchese, T. Morishita, and K. Ueda, Extracting Electron-Ion Differential Scattering Cross Sections for Partially Aligned Molecules by Laser-Induced Rescattering Photoelectron Spectroscopy, Phys. Rev. Lett. **106**, 063001 (2011).

[29] A. Gazibegović-Busuladžić, E. Hasović, M. Busuladžić, D. B. Milošević, F. Kelkensberg, W. K. Siu, M. J. J. Vrakking, F. Lépine, G. Sansone, M. Nisoli, I. Znakovskaya, and M. F. Kling, Above-threshold ionization of diatomic molecules by few-cycle laser pulses, Phys. Rev. A **84**, 043426 (2011).

[30] C. I. Blaga, J. Xu, A. D. DiChiara, E. Sistrunk, K. Zhang, P. Agostini, T. A. Miller, L. F. DiMauro, and C. D. Lin, Imaging ultrafast molecular dynamics with laser-induced electron diffraction, Nature (London) **483**, 194 (2012).

[31] M. G. Pullen, B. Wolter, A.-T. Le, M. Baudisch, M. Hemmer, A. Senftleben, C. D. Schröter, J. Ullrich, R. Moshammer, C. D. Lin, and J. Biegert, Imaging an aligned polyatomic molecule with laser-induced electron diffraction, Nat. Commun. **6**, 7262 (2015).

[32] W. Quan, X. Hao, X. Hu, R. Sun, Y. Wang, Y. Chen, S. Yu, S. Xu, Z. Xiao, X. Lai, X. Li, W. Becker, Y. Wu, J. Wang, X. Liu, and J. Chen, Laser-Induced Inelastic Diffraction from Strong-Field Double Ionization, Phys. Rev. Lett. **119**, 243203 (2017).

[33] C. D. Lin, A.-T. Le, C. Jin, and H. Wei, Elements of the quantitative rescattering theory, J. Phys. B **51**, 104001 (2018).

[34] S. G. Walt, N. B. Ram, M. Atala, N. I. Shvetsov-Shilovski, A. von Conta, D. Baykusheva, M. Lein, and H. J. Wörner, Dynamics of valence-shell electrons and nuclei probed by strong-field holography and rescattering, Nat. Commun. **8**, 15651 (2017).

[35] F. Schell, T. Bredtmann, C. P. Schulz, S. Patchkovskii, M. J. J. Vrakking, and J. Mikosch, Molecular orbital imprint in laser-driven electron recollision, Sci. Adv. **4**, eaap8148 (2018).

[36] O. I. Tolstikhin and T. Morishita, Adiabatic theory of ionization by intense laser pulses: Finite-range potentials, Phys. Rev. A **86**, 043417 (2012).

[37] T. Morishita and O. I. Tolstikhin, Adiabatic theory of strong-field photoelectron momentum distributions near a backward rescattering caustic, Phys. Rev. A **96**, 053416 (2017).

[38] P. A. Batishchev, O. I. Tolstikhin, and T. Morishita, Atomic Siegert states in an electric field: Transverse momentum distribution of the ionized electrons, Phys. Rev. A **82**, 023416 (2010).

[39] O. I. Tolstikhin, T. Morishita, and L. B. Madsen, Theory of tunneling ionization of molecules: Weak-field asymptotics including dipole effects, Phys. Rev. A **84**, 053423 (2011).

[40] R. G. Newton, *Scattering Theory of Waves and Particles* (Springer-Verlag, New York, 1982).

[41] G. G. Paulus, W. Becker, W. Nicklich, and H. Walther, Rescattering effects in above-threshold ionization: A classical model, J. Phys. B **27**, L703 (1994).

[42] H. Geiseler, N. Ishii, K. Kaneshima, F. Geier, T. Kanai, O. I. Tolstikhin, T. Morishita, and J. Itatani, Carrier-envelope phase mapping in laser-induced electron diffraction, Phys. Rev. A **94**, 033417 (2016).

[43] Y. Ito, M. Okunishi, T. Morishita, O. I. Tolstikhin, and K. Ueda, Rescattering photoelectron spectroscopy of heterodiatomic molecules with an analytical returning photoelectron wave packet, Phys. Rev. A **97**, 053411 (2018).

[44] T. Morishita, Z. Chen, S. Watanabe, and C. D. Lin, Two-dimensional electron momentum spectra of argon ionized by short intense lasers: Comparison of theory with experiment, Phys. Rev. A **75**, 023407 (2007).

[45] O. I. Tolstikhin, S. Watanabe, and M. Matsuzawa, "Slow" variable discretization: A novel approach for Hamiltonians allowing adiabatic separation of variables, J. Phys. B **29**, L389 (1996).

[46] K. Baluja, P. Burke, and L. Morgan, *R*-matrix propagation program for solving coupled second-order differential equations, Comput. Phys. Commun. **27**, 299 (1982).

[47] V. H. Trinh, O. I. Tolstikhin, L. B. Madsen, and T. Morishita, First-order correction terms in the weak-field asymptotic theory of tunneling ionization, Phys. Rev. A **87**, 043426 (2013).

[48] R. H. Garvey, G. H. Jackman, and A. E. S. Green, Independent-particle-model potentials for atoms and ions with $36 < Z \leqslant 54$ and a modified Thomas-Fermi atomic energy formula, Phys. Rev. A **12**, 1144 (1975).

[49] J. A. R. Samson and J. L. Gardner, On the ionization potential of molecular oxygen, Can. J. Phys. **53**, 1948 (1975).

[50] R. Cireasa, A. E. Boguslavskiy, B. Pons, M. C. H. Wong, D. Descamps, S. Petit, H. Ruf, N. Thiré, A. Ferré, J. Suarez, J. Higuet, B. E. Schmidt, A. F. Alharbi, F. Légaré, V. Blanchet, B. Fabre, S. Patchkovskii, O. Smirnova, Y. Mairesse, and V. R. Bhardwaj, Probing molecular chirality on a sub-femtosecond timescale, Nat. Phys. **11**, 654 (2015).

[51] Y. Harada, E. Haraguchi, K. Kaneshima, and T. Sekikawa, Circular dichroism in high-order harmonic generation from chiral molecules, Phys. Rev. A **98**, 021401(R) (2018).

[52] D. Baykusheva and H. J. Wörner, Chiral Discrimination Through Bielliptical High-Harmonic Spectroscopy, Phys. Rev. X **8**, 031060 (2018).